Article:
Yang, W. orcid.org/0000-0001-8398-4014, Lv, X., Wang, L. et al. (2 more authors) (2023) A DEM–CFD coupling method for modelling two-hole synchronous hydraulic fracturing. Geomechanics and Geophysics for Geo-Energy and Geo-Resources, 9 (1). 6. ISSN 2363-8419

https://doi.org/10.1007/s40948-023-00556-w

Geomech. Geophys. Geo-energ. Geo-resour. (2023) 9:6
https://doi.org/10.1007/s40948-023-00556-w

ORIGINAL ARTICLE

A DEM–CFD coupling method for modelling two-hole synchronous hydraulic fracturing

Wendong Yang · Xianxian Lv · Lige Wang · Di Peng · Xizhong Chen

Received: 12 April 2022 / Accepted: 27 November 2022

Abstract This work introduced a novel numerical approach for modelling hydraulic fracturing processes. The Edinburgh bonded particle model was employed to establish the discrete element model of the rock samples, and it was further coupled with computational fluid dynamics to simulate the hydraulic fracturing. The fracture propagation law was taken into account under various principal stress differences to confirm the viability of the model. In addition, the model was used to investigate the fracture propagation mechanism of two-hole synchronous hydraulic fracturing. The results indicate that the arrangement and spacing of two holes will affect the complexity of hydraulic fractures. The principal stress difference becomes more prominent in the direction of hydraulic fracture propagation with the increase in the principal stress difference.

Highlights

- The Edinburgh Bonded Particle Model (EBPM) is employed to establish the discrete element model.
- The DEM-CFD coupling method is employed to model two holes synchronous hydraulic fracturing.
- The hole arrangement mode, spacing between two holes and principal stress difference affect the fractures propagation.

Keywords DEM–CFD · Two holes · Synchronous hydraulic fracturing · Fracture propagation

1 Introduction

Hydraulic fracturing is a technology that can expand the fracture in the rock stratum by pumping high-pressure fluid. It has been extensively utilized in deep energy exploitation, such as enhanced geothermal systems, shale gas exploitation, and the exploitation and

W. Yang (✉) · X. Lv
College of Pipeline and Civil Engineering, China University of Petroleum, D Building, Qingdao 266580, Shandong, People's Republic of China
e-mail: wendongy@gmail.com; yangwd@upc.edu.cn

X. Lv
e-mail: lvxxian@163.com

L. Wang · X. Chen
Department of Chemical and Biological Engineering, University of Sheffield, Sheffield, UK
e-mail: barcelonawlg@gmail.com

X. Chen
e-mail: xizhong.chen@sheffield.ac.uk

D. Peng
Shenzhen Research Institute of Shandong University, Shenzhen 518057, Guangdong, People's Republic of China
e-mail: di_peng@outlook.com

D. Peng
Ubiquitous Particles, Twickenham, London, UK

Published online: 14 February 2023

stimulation of unconventional oil and gas reservoirs (Liu et al. 2016; Detournay 2016; Zhang et al. 2019b).

In the 1950s, the first hydraulic fracturing model was proposed. KGD (Geertsma et al. 1969; Khristianovich et al. 1955) and PKN (Nordgren 1972; Perkins et al. 1961) are two main models, which are based on the constant height assumption. Yew et al. (2014) found that hydraulic fractures can be characterized by KGD under uniform in situ stress, while they can be characterized by PKN under uneven in situ stress. Hubbert et al. (1957) derived the first fracture failure formula and revealed the propagation direction of hydraulic fracture.

However, theoretical analysis cannot address the complex conditions encountered in hydraulic fracturing field operation because of the complex stress state and heterogeneity of deep rock masses. Many factors, such as natural fractures (Li et al. 2020), in situ stress (Liu et al. 2021a) and viscosity of the fluid (Krzaczek et al. 2020), can affect the development of hydraulic fractures. Numerous researchers have utilized numerical simulations and laboratory tests to investigate the fracture propagation process to comprehend the impact of these factors.

Cylindrical and cube samples are usually used for hydraulic fracturing laboratory tests. In terms of sample selection, it is divided into natural materials (Lei et al. 2021), such as clay (Xu et al. 2015) granite, (Li et al. 2019), sandstone (Zheng et al. 2020b), coal (Liu et al. 2021a) and artificial materials such as cement mortar, which can be poured through a certain mix proportion (Shi et al. 2021). The researchers studied the effect of stress, type and rate of injected fluid, natural fracture, borehole diameter and perforation azimuth. The results show that all the factors have great influences on the development of hydraulic fractures. Although several groups of comparative tests are designed, there may exist some errors in the experimental results due to the heterogeneity of samples, especially in the aspect of hydraulic fracture propagation.

Numerical simulation is a common method to study the mechanical behaviour of rock. For instance, Xu et al. (2018) investigated the complex time-dependent behaviour of heterogeneous brittle rocks under coupled hydromechanical loading using the finite element method. Xu et al. (2020) studied the mechanical behaviour and failure mode of rock as well as its damage evolution on the particle scale with the discrete element method. In the latest research, Zhou et al. (2022) proposed an improved grain-based numerical manifold method (NMM) to study the deformation, damage and fracturing of rock at the mesoscale. These numerical simulation methods are also applied to hydraulic fracturing, such as the FEM (Ni et al. 2020; Rueda et al. 2020), XFEM (Wang et al. 2018; Zheng et al. 2020a; Zou et al. 2020; Liu et al. 2021b) and DEM (Krzaczek et al. 2020; Zhang et al. 2019a; Li 2020). In the aspect of single-hole hydraulic fracturing simulation, a model size consistent with the laboratory scale is considered. Additionally, more factors can be studied in the numerical simulation. For example, the propagation law of hydraulic fractures in the presence of natural fractures is simulated based on the CFD−DEM method (Li et al. 2020). Hydromechanical coupled modelling of hydraulic fracturing has also been investigated (Cheng et al. 2020).

In addition, researchers also simulated two-hole synchronous hydraulic fracturing. Duan et al. (2020) evaluated the effect of injection parameters and rock stratum conditions on the propagation of multiple hydraulic fractures induced simultaneously and investigated the effect of stress shadowing. Yang et al. (2021) investigated the fracture propagation mechanism of two-hole hydraulic fracturing under different factors. The simulation results have the potential for optimizing the perforation design layout in hydraulic fracturing operations.

In summary, much research has been conducted on the factors that influence the development of single-hole hydraulic fracturing. However, dual hole synchronous hydraulic fracturing is less studied by discrete element method, and a very thorough research technique has not been developed. This work presents a novel numerical simulation method of hydraulic fracturing. The discrete element model of the rock sample was established based on the Edinburgh bonded particle model. The hydraulic fracturing process was simulated using the DEM–CFD coupling technique. The feasibility of the hydraulic fracturing model was verified by considering the fracture propagation law under different principal stress differences. To explore the fracture propagation mechanism of two-hole synchronous hydraulic fracturing, a numerical model of two-hole hydraulic fracturing was established.

2 Edinburgh bonded particle model

The Hertz–Mindlin with bonding model, the built-in bonding model of EDEM, has the following shortcomings. The shear stiffness and normal stiffness of the

model and the cross-sectional area of the bond cannot be changed once they are determined in the calculation process. The above shortcomings will cause inaccurate calculation results. This can cause significant errors. The Edinburgh bonded particle model (EBPM) overcomes the above shortcomings. EBPM was first proposed and verified by Nicholas John Brown, which can accurately reflect the mechanical behaviour of cementitious materials (Brown 2013; Brown et al. 2014). A large number of numerical simulation tests have been carried out to verify its applicability in concrete materials. The effects of the parameters in the EBPM on Young's modulus, compressive strength and failure mode are analysed. Only one contact model can exist between particles in the EBPM model, that is, bonded contact model (Timoshenko beam bonded-contact model) or nonbonded contact model (Hertz−Mindlin contact model). The bond can transfer shear force, axial force and bending moment. Figure 1 shows the composition of the EBPM.

At the bonded contact, the Timoshenko beam bonded-contact model (TBBM) is adopted. This model assumes that there was a virtual bond element existing between the particles. The constitutive behaviour of the bond is based on Timoshenko beam element theory (Timoshenko 1922). At the nonbonded contact, the Hertz−Mindlin contact model (HMCM) is adopted. In this model, the normal force model and the tangential force model is based on the work of Hertzian (Hertz 1882) and Mindlin (Mindlin 1949; Mindlin et al. 1953) respectively. TBBM can calculate compressive stress, tensile stress, shear stress and bending, while HMCM can only calculate compressive stress and shear stress. The specific description of the two contact models will be expanded below.

2.1 The Timoshenko beam bonded-contact model

The primary component of the EBPM is the TBBM. The mechanical behaviour of each bond is presumed to be comparable to that of the Timoshenko beam in the TBBM model (Timoshenko 1922). Rigidity is thought to exist between each end of the bond and particle. As a result, each end of the bond and the particle have the identical six degrees of freedom.

The position of the connected particles affects the geometric characteristics of the bond. r_b is the cross-sectional radius of the bond.

$$r_b = \lambda \cdot \min\left(r_A, r_B\right) \tag{1}$$

where λ is the bond radius multiplier, r_A and r_B are the radii of particles A and B, respectively.

The relationship between internal force and displacement is the core of Timoshenko beam theory. Only the particle mass is considered in the calculation. The displacement increment of the bond is obtained according

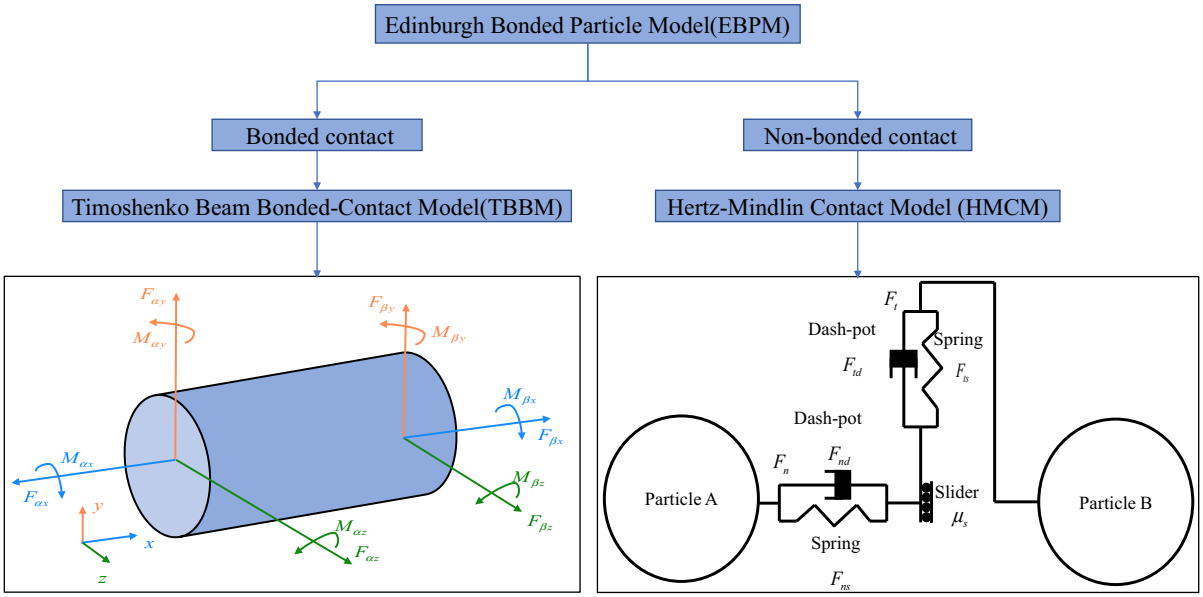

Fig. 1 The composition of the EBPM

to the change of particle position due to the rigid connection between bond and particle. The internal force increment of the bond can be obtained from Eq. (2) in each time step.

$$\{\Delta F\}=[K]\cdot\{\Delta\mu\} \tag{2}$$

where $\{\Delta\mu\}$ and $\{\Delta F\}$ are the displacement increment and the force increment, respectively, and $[K]$ is tangential stiffness matrix, following Eq. (5). Each force and displacement have two subscripts as shown in Fig. 2. α or β represents the two ends of the bond, and x, y, or z represents the direction of the force.

$$\begin{aligned}\{\Delta F\}=\{&\Delta F_{\alpha x}\ \Delta F_{\alpha y}\ \Delta F_{\alpha z}\ \Delta M_{\alpha x}\ \Delta M_{\alpha y}\ \Delta M_{\alpha z}\\ &\Delta F_{\beta x}\ \Delta F_{\beta y}\ \Delta F_{\beta z}\ \Delta M_{\beta x}\ \Delta M_{\beta y}\ \Delta M_{\beta z}\}\end{aligned} \tag{3}$$

$$\begin{aligned}\{\Delta\mu\}=\{&\Delta d_{\alpha x}\ \Delta d_{\alpha y}\ \Delta d_{\alpha z}\ \Delta\theta_{\alpha x}\ \Delta\theta_{\alpha y}\ \Delta\theta_{\alpha z}\\ &\Delta d_{\beta x}\ \Delta d_{\beta y}\ \Delta d_{\beta z}\ \Delta\theta_{\beta x}\ \Delta\theta_{\beta y}\ \Delta\theta_{\beta z}\}\end{aligned} \tag{4}$$

where A_b is the bond's cross-sectional area, Φ is the Timoshenko shear coefficient, E_b is the Young's modulus of bond, and I_b is the bond's second moment of area where:

$$I_b=\frac{r_b\pi}{4} \tag{6}$$

$$A_b=r_b^2\pi \tag{7}$$

$$\Phi=\frac{f_s 12E_bI_b}{G_bA_bL_b^2}=\frac{20r_b^2(1+\nu_b)}{3L_b^2} \tag{8}$$

where G_b is the bond shear modulus, f_s is the form factor for shear, and r_b is the bond radius.

2.2 Failure criteria of bonds

In the TBBM, the ultimate stress can be calculated by Eqs. (9), (10) and (11).

$$\sigma_C=S_C\cdot((\varsigma_C\cdot N)+1) \tag{9}$$

$$[K]=\begin{bmatrix}
\frac{E_bA_b}{L_b} & & & & & & & & & & & \\
0 & \frac{12E_bI_b}{L_b^3(1+\Phi)} & & & & & & & & & & \\
0 & 0 & \frac{12E_bI_b}{L_b^3(1+\Phi)} & & & & & & & \text{Symmetric} & & \\
0 & 0 & 0 & \frac{E_bI_b}{(1+\nu_b)L_b} & & & & & & & & \\
0 & 0 & \frac{-6E_bI_b}{L_b^2(1+\Phi)} & 0 & \frac{(4+\Phi)E_bI_b}{L_b(1+\Phi)} & & & & & & & \\
0 & \frac{6E_bI_b}{L_b^2(1+\Phi)} & 0 & 0 & 0 & \frac{(4+\Phi)E_bI_b}{L_b(1+\Phi)} & & & & & & \\
\frac{-E_bA_b}{L_b} & 0 & 0 & 0 & 0 & 0 & \frac{E_bA_b}{L_b} & & & & & \\
0 & \frac{-12E_bI_b}{L_b^3(1+\Phi)} & 0 & 0 & 0 & \frac{-6E_bI_b}{L_b^2(1+\Phi)} & 0 & \frac{12E_bI_b}{L_b^3(1+\Phi)} & & & & \\
0 & 0 & \frac{-12E_bI_b}{L_b^3(1+\Phi)} & 0 & \frac{6E_bI_b}{L_b^2(1+\Phi)} & 0 & 0 & 0 & \frac{12E_bI_b}{L_b^3(1+\Phi)} & & & \\
0 & 0 & 0 & \frac{-E_bI_b}{(1+\nu_b)L_b} & 0 & 0 & 0 & 0 & 0 & \frac{E_bI_b}{(1+\nu_b)L_b} & & \\
0 & 0 & \frac{-6E_bI_b}{L_b^2(1+\Phi)} & 0 & \frac{(2-\Phi)E_bI_b}{L_b(1+\Phi)} & 0 & 0 & 0 & \frac{6E_bI_b}{L_b^2(1+\Phi)} & 0 & \frac{(4+\Phi)E_bI_b}{L_b(1+\Phi)} & \\
0 & \frac{6E_bI_b}{L_b^2(1+\Phi)} & 0 & 0 & 0 & \frac{(2-\Phi)E_bI_b}{L_b(1+\Phi)} & 0 & \frac{-6E_bI_b}{L_b^2(1+\Phi)} & 0 & 0 & 0 & \frac{(4+\Phi)E_bI_b}{L_b(1+\Phi)}
\end{bmatrix} \tag{5}$$

$$\sigma_T=S_T\cdot((\varsigma_T\cdot N)+1) \tag{10}$$

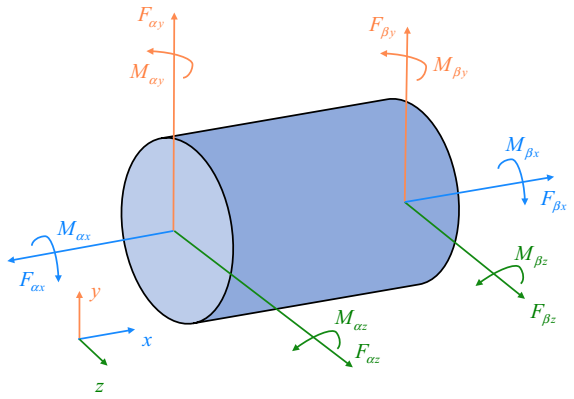

Fig. 2 Forces and moments at both ends of the bond

$$\tau = S_S \cdot ((\varsigma_S \cdot N) + 1) \tag{11}$$

where σ_C, σ_T, τ are the ultimate compressive, tensile, shear strength of bond, respectively, S_C, S_T, S_S are the mean bond compressive, tensile, shear strength, respectively, ς_C, ς_T, ς_S are the coefficient of variation of compressive, tensile, shear strength, respectively, N is a random number.

Assuming that each bond is linear, elastic and brittle, the maximum compressive stress in the bond can be calculated by Eqs. (12) and (13).

$$\sigma_{Ci} = \left(\frac{F_{\beta x}}{A_b} - \frac{r_b \sqrt{M_{iy}^2 + M_{iz}^2}}{I_b} \right) \quad i = \alpha, \beta \tag{12}$$

$$\sigma_{CMAX} = -\min\left(\sigma_{C\alpha}, \sigma_{C\beta}\right) \tag{13}$$

The maximum tensile stress in the bond can be calculated by Eqs. (14) and (15).

$$\sigma_{Ti} = \left(\frac{F_{\beta x}}{A_b} + \frac{r_b \sqrt{M_{iy}^2 + M_{iz}^2}}{I_b} \right) \quad i = \alpha, \beta \tag{14}$$

$$\sigma_{TMAX} = -\max\left(\sigma_{T\alpha}, \sigma_{T\beta}\right) \tag{15}$$

Equation (16) is the formula for calculating the maximum shear stress.

$$\tau_{MAX} = \frac{|M_{\alpha x}| r_b}{2I_b} + \frac{4\sqrt{F_{\alpha y}^2 + F_{\alpha z}^2}}{3A_b} \tag{16}$$

The bond failure criteria are as follows:

$$\tau_{MAX} > \tau \tag{17}$$

$$\sigma_{TMAX} > \sigma_T \tag{18}$$

$$\sigma_{CMAX} > \sigma_C \tag{19}$$

where τ_{MAX}, σ_{CMAX}, and σ_{TMAX} are the maximum shear, tensile, and compressive strengths, respectively.

2.3 The Hertz−Mindlin contact model

The Hertz−Mindlin contact model is adopted for the nonbonded contact model between particles (Fig. 3). In this model, the normal force model and the tangential force model is based on the work of Hertzian (1882) and Mindlin (1949, 1953) respectively.

The normal force and tangential force are obtained from the following formula.

$$F_n = F_{ns} + F_{nd} \tag{20}$$

$$F_t = F_{ts} + F_{td} \tag{21}$$

F_{ns} is the function of normal overlap, which can be calculated by Eq. (22).

$$F_{ns} = \frac{4}{3} E^* \sqrt{r^*} \delta_n^{1.5} \tag{22}$$

$$\frac{1}{E^*} = \frac{1 - \nu_A^2}{E_A} + \frac{1 - \nu_B^2}{E_B} \tag{23}$$

$$r^* = \frac{r_A \cdot r_B}{r_A + r_B} \tag{24}$$

in which r^* and E^* are the equal radius and equivalent Young's modulus, respectively, and ν_A, E_A, r_A, ν_B, E_B and r_B are the Poisson's ratio, Young's modulus and radius of the two particles, respectively.

The normal damping force is calculated by Eq. (25).

$$F_{nd} = -2\sqrt{\frac{5}{6}} b_d \sqrt{S_n m^*} V_{n,rel} \tag{25}$$

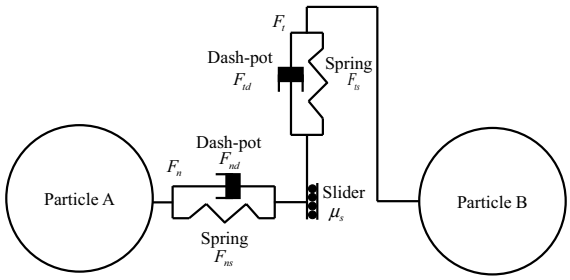

Fig. 3 The Hertz-Middlin contact model

$$b_d = \frac{\ln e}{\sqrt{\ln^2 e + \pi^2}} \tag{26}$$

$$m^* = \frac{m_A \cdot m_B}{m_A + m_B} \tag{27}$$

$$S_n = 2E^* \sqrt{r^* \delta_n} \tag{28}$$

where m^* is the equivalent mass, b_d is a damping ratio, $V_{n,rel}$ is the normal component of the relative velocity and S_n is the normal stiffness.

$$F_{ts} = -S_t \delta_t \tag{29}$$

$$F_{td} = -2\sqrt{\frac{5}{6}} b_d \sqrt{S_t m^*} V_{t,rel} \tag{30}$$

$$S_t = 8G^* \sqrt{r^* \delta_n} \tag{31}$$

$$\frac{1}{G^*} = \frac{1 - \nu_A^2}{G_A} + \frac{1 - \nu_B^2}{G_B} \tag{32}$$

in which $V_{t,rel}$ is the tangential component of the relative velocity, G^* is the equivalent modulus and S_t is the tangential stiffness.

3 Coupling mechanism and hydraulic fracturing model

3.1 Coupling mechanism

In this work, we propose the CFD−DEM coupling method to simulate hydraulic fracturing. The particle motion and fluid flow were simulated by EDEM and Fluent, respectively. We connect the two software programs through a coupling interface that can transmit data between them. The initialization of flow field in fluent is the first step of coupling calculation where the flow field information can been obtained by solving the Navier–Stokes equation and momentum equation. The coupling force of fluid to particles will be transferred to EDEM through the coupling interface. Then the particle velocity, displacement and other information will be obtained in EDEM through Newton's second law. Fluent obtains the information and continues the next iterative calculation. The above process will be repeated until a convergent solution is obtained. The CFD−DEM coupling process is shown in Fig. 4.

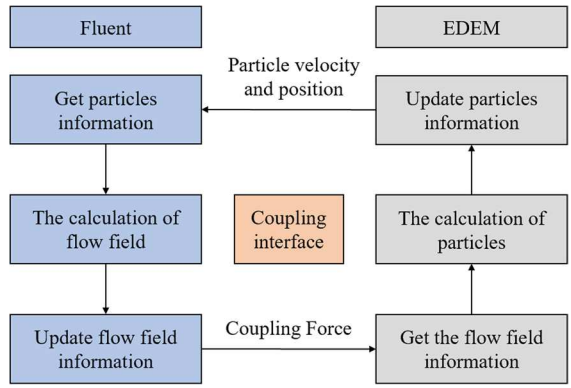

Fig. 4 The CFD−DEM coupling process

3.1.1 CFD calculation principle

Eulerian multiphase flow model was selected to simulate the interaction between different phases in this model, fluid and solid occupy a certain volume, which can be expressed in volume fraction. To solve the problem of volume fraction, the dense discrete phase model (DDPM) in Eulerian multiphase flow was introduced. In DDPM, the particle phase and fluid phase occupy part of the volume of a fluent grid. The volume fraction of each phase is added to 1. Fluid−solid coupling is realized through interphase force. In this work, the interphase force refers to the drag force. For fluid flow, the governing equations are shown in Eqs. (33) and (34):

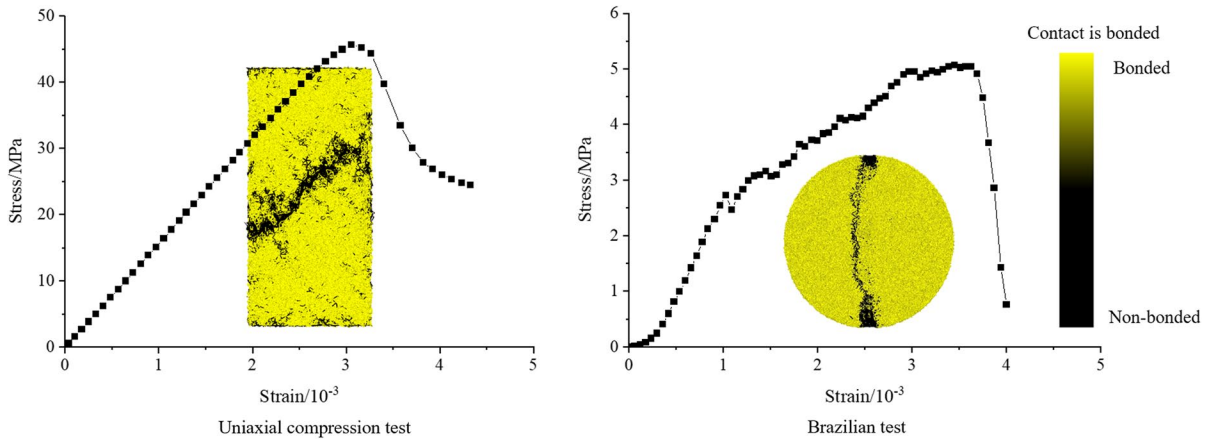

Fig. 5 Failure mode and stress−strain curve

$$\frac{\partial(\alpha_l\rho_l)}{\partial t}+\nabla\cdot(\alpha_l\rho_l v_l)=0 \tag{33}$$

$$\frac{\partial(\alpha_l\rho_l v_l)}{\partial t}+\nabla\cdot(\alpha_l\rho_l v_l v_l)=-\alpha_l\nabla p+\nabla\cdot\bar{\bar{\tau}}+\alpha_l\rho_l g+K_{pl}(v_p-v_l)+\sum F_l \tag{34}$$

where ρ_l is the density of fluid, α_l is the volume fraction of fluid, $\bar{\bar{\tau}}$ is the stress tensor, K_{pl} is the exchange coefficient, v_l is the velocity of fluid, and v_p is the velocity of particles.

The Gidaspow model (Gidaspow 1994) is selected as the drag model.

When $\alpha_l>0.8$, the liquid−solid exchange coefficient is obtained from Eq. (35):

$$K_{pl}=\frac{3}{4}C_D\frac{\alpha_s\alpha_l\rho_l|v_s-v_l|}{d_s}\alpha_l^{-2.65} \tag{35}$$

$$C_D=\frac{24}{\alpha_l\mathrm{Re}_s}\left[1+0.15(\alpha_l\mathrm{Re}_s)^{0.687}\right] \tag{36}$$

when $\alpha_l<0.8$, the liquid−solid exchange coefficient is obtained from Eq. (37):

$$K_{pl}=150\frac{\alpha_s(1-\alpha_l)\mu_l}{\alpha_l d_s^2}+1.75\frac{\rho_l\alpha_s|v_s-v_l|}{d_s} \tag{37}$$

3.1.2 DEM calculation principle

EDEM can calculate the interaction between particles and the external force applied to the particles. In the discrete element simulation, the acceleration is calculated using Newton's second law. The motion equation of particles at a certain time can be obtained as follows:

$$\left.\begin{aligned} m\tfrac{dv}{dt}&=\sum F\\ I\tfrac{d\omega}{dt}&=\sum M\end{aligned}\right\} \tag{38}$$

where $\sum F$ and $\sum M$ is the resultant force and moment, respectively, v and ω is the translational and angular velocity of particles, respectively, m is the mass of particles, t is the time, and I is the moment of inertia.

The particle velocities and locations are updated by numerically integrating the accelerations throughout a time step.

$$\left.\begin{aligned} v(t+\Delta t)&=v(t)+\tfrac{dv}{dt}\Delta t\\ u(t+\Delta t)&=u(t)+v(t)\Delta t\end{aligned}\right\} \tag{39}$$

$$\left.\begin{aligned} \omega(t+\Delta t)&=\omega(t)+\tfrac{d\omega}{dt}\Delta t\\ \theta(t+\Delta t)&=\theta(t)+\omega(t)\Delta t\end{aligned}\right\} \tag{40}$$

Table 1 Comparison table of macroparameters between the laboratory test and numerical simulation

Macroparameters	Laboratory	Numerical	Error (%)
Compressive strength/MPa	45.24	45.67	0.95
Tensile strength/MPa	5.12	5.06	1.17
Young's modulus/GPa	15.64	15.86	1.41

3.2 Parameter calibration and numerical model establishment

3.2.1 Calibration of parameters

The constitutive parameters of rock, such as compressive strength, Poisson's ratio and Young's modulus, can be obtained through laboratory tests. However, the contact parameters of particles in discrete element analysis cannot be obtained directly. They often need to be calibrated through virtual tests. In this work, the microparameters of rock materials are calibrated by uniaxial compression tests and Brazilian tests. A previous study demonstrated that mean bond shear, tensile, compressive strength and the bond Young's modulus are more important than others affecting the compressive strength and Young's modulus (Brown 2013). In this work, we calibrated the bond Young's modulus and mean bond shear, tensile, compressive strength. The macroscopic mechanical parameters of rock materials refer to the hydraulic fracturing test of Yang et al. (2020).

Based on EDEM, we have established two samples, whose dimensions are Φ 100 mm × 200 mm and Φ 50 mm × 25 mm. The loading rate is 0.1 m/s. The particle size follows a uniform distribution, and the minimum and maximum radii of the particles were 0.5 mm and 2 mm, respectively. Figure 5 demonstrates the stress–strain curve and failure mode of the two specimens following parameter calibration. Table 1 shows the comparison table of macroparameters between the laboratory test and numerical simulation. The consequences of the numerical simulation and those of the laboratory tests coincide fairly well. Table 2 depicts the meso-parameters of the EBPM.

Table 2 The meso-parameters of the EBPM

Meso-parameters	Unite	Value
Particle		
Density	kg/m^3	2500
Young's modulus	GPa	40
Poisson's ratio	–	0.28
Minimum radius	mm	0.5
Maximum radius	mm	2
Loading plate		
Density	kg/m^3	7850
Young's modulus	GPa	200
Poisson's ratio	–	0.3
Particle–particle		
Coefficient of restitution	–	0.5
Coefficient of static friction	–	0.5
Coefficient of rolling friction	–	0.5
Particle-loading plate		
Coefficient of restitution	–	0.0001
Coefficient of static friction	–	1
Coefficient of rolling friction	–	0
Bond		
Young's modulus	GPa	22.5
Poisson's ratio	–	0.2
Mean bond compressive strength	MPa	320
Mean bond tensile strength	MPa	67.5
Mean bond shear strength	MPa	67.5
Coefficient of variation of compressive strength	–	0
Coefficient of variation of compressive strength	–	0
Coefficient of variation of compressive strength	–	0
Contact radius multiplier	–	1.1
Bond radius multiplier	–	1

3.2.2 Verification of the hydraulic fracturing model

We established the discrete model and CFD model with the same size. As shown in Fig. 6, the size of the model was 300 mm × 300 mm × 10 mm. There was a water injection hole with a diameter of 25 mm in the centre of the model. There were 50,980 particles being generated in the end for the discrete model. For the CFD model, a total of 2066 fluid grids were generated. The fluid was injected at a rate of 16 m/s in the injection hole.

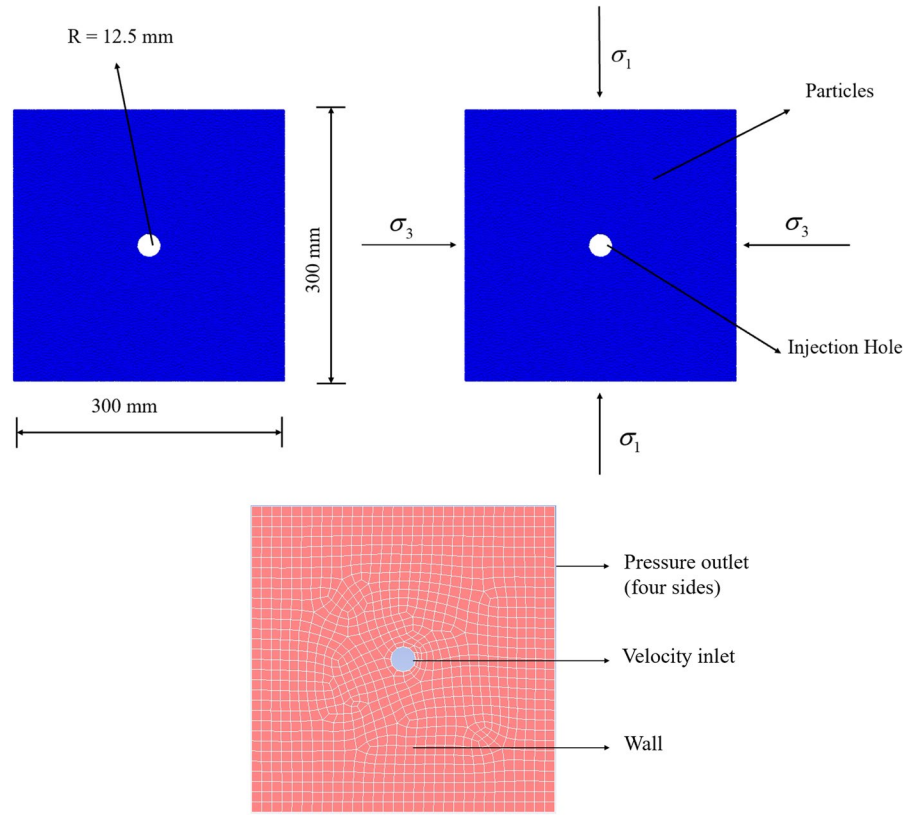

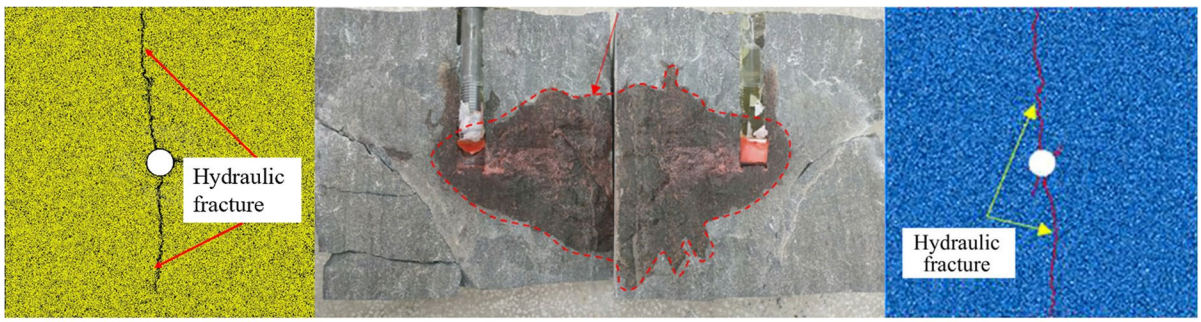

Hydraulic fracturing by DEM-CFD coupling by the present study

Laboratory test after Yang et al. 2020

DEM simulation by Yang et al. 2020

Fig. 6 Discrete element numerical and CFD numerical models

Fig. 7 The fracture propagation pattern of hydraulic fracturing

Table 3 Hydraulic fracturing experimental conditions

Conditions	1	2	3	4	5
σ_1(MPa)	4	8	12	16	20
σ_3(MPa)	4	4	4	4	4
$\sigma_1 - \sigma_3$(MPa)	0	4	8	12	16

In the numerical simulation, stresses of 2 and 4 MPa are applied to the X and Y directions of the discrete model, respectively. The fracture propagation pattern of hydraulic fracturing is shown in Fig. 7. The fracture propagated along the maximum stress direction, which is the same as the result of Yang's

Table 4 The bond parameters of the EBPM

Bond parameters	Unite	Value
Young's modulus	GPa	57
Poisson's ratio	–	0.2
Mean bond compressive strength	MPa	1000
Mean bond tensile strength	MPa	230
Mean bond shear strength	MPa	230
Coefficient of variation of compressive strength	–	0
Coefficient of variation of compressive strength	–	0
Coefficient of variation of compressive strength	–	0
Bond radius multiplier	–	1

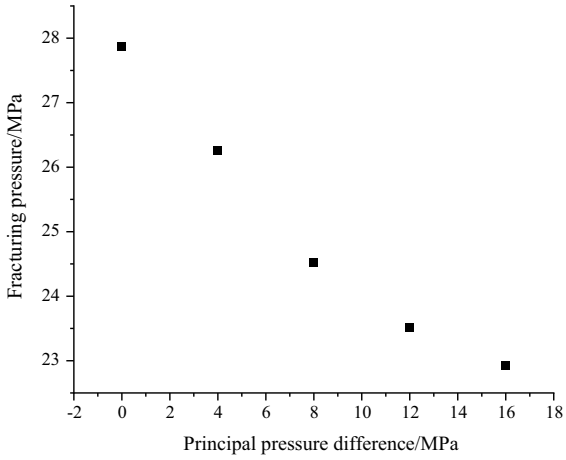

Fig. 8 The value of fracturing pressure under different principal stress differences

numerical simulation and laboratory test. Our simulation results are consistent with the existing research results (Duan et al. 2018; Cheng et al. 2020; Yang et al. 2020). The breaking pressure is 11.37 MPa, while Yang's laboratory result is 11.48 MPa (Yang et al. 2020). Therefore, the DEM–CFD coupling method can well simulate hydraulic fracturing.

4 Numerical simulation of hydraulic fracturing

4.1 Effect of different principal stress differences on single-hole hydraulic fracturing

Table 3 shows the hydraulic fracturing experimental conditions. Another rock material was chosen for study to verify the adaptability of the model. The uniaxial compressive strength was 152 MPa, the tensile strength was 18.54 MPa, Young's modulus was 39.99 GPa (Cheng et al. 2020). The particle size follows a uniform distribution, and the minimum and maximum radii of the particles were 0.5 mm and 2 mm, respectively. After parameter calibration, the bond parameters are shown in Table 4. The fluid was injected at a rate of 33 m/s. The size of the model was 300 mm × 300 mm × 10 mm. There was a water injection hole with a diameter of 20 mm in the centre of the model.

Figure 8 shows the value of fracturing pressure under different principal stress differences. Under the condition of the principal stress difference is zero, the maximum fracturing pressure is 27.88 MPa. Crack fracturing pressure will decrease as the principal stress difference rises. The minimum fracturing pressure is 22.93 MPa.

Figure 9 shows the fractures propagation process under different principal stress differences. It can be observed that under the condition of the principal stress difference was zero, the fracture will first appear at the upper right of the water injection hole in the initial stage of hydraulic fracturing. With the continuous injection of fluid, four hydraulic fractures appeared. Among them, the two hydraulic fractures on the right side of the injection hole developed rapidly.

When the principal stress difference was 4 MPa, three hydraulic fractures are generated around the hole in the initial stage of simulation, two of which expand rapidly with the injection of fluid. At approximately 0.001 s, a fourth hydraulic fracture was found. It expanded horizontally during the fracturing process and finally reached the edge of the model. Among the three hydraulic cracks generated in the initial stage of simulation, there was one hydraulic crack that has not expanded in the whole simulation process.

The inverted Y-type fracture propagation model appears when the principal stress was 8 MPa. The three hydraulic cracks all grow rapidly. The direction of hydraulic cracks in the upper part of the water injection hole consistent with the direction of maximum principal stress. The two hydraulic fractures in the lower part of the water injection hole also show the trend of expanding along the direction of maximum principal stress.

The direction of two main hydraulic cracks is completely affected by the maximum principal

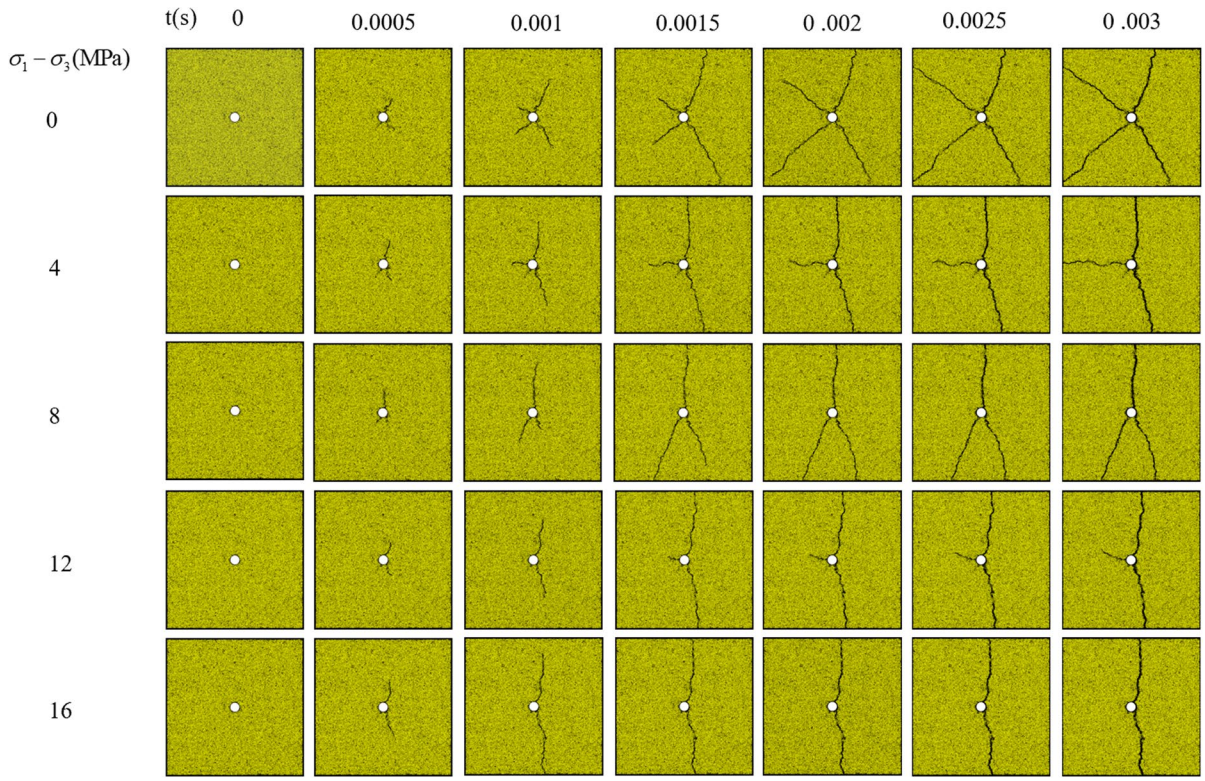

Fig. 9 The fracture propagation process of hydraulic fracturing under different principal stress differences

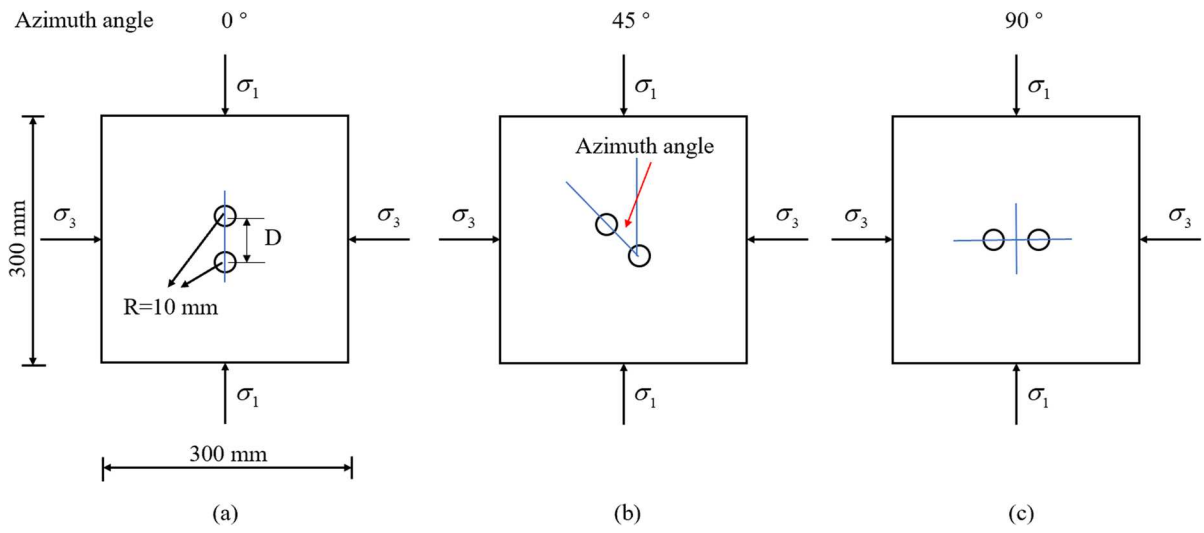

Fig. 10 Schematic diagram of three different hole arrangement modes

stress under the condition of the principal stress difference was 12 MPa. At approximately 0.0015 s, another fracture appears as the main fractures extend to the edge of the model. However, this hydraulic fracture develops slowly. It did not develop to the edge of the model until the end of the simulation. In the condition of the principal stress was 20 MPa, there are only two hydraulic fractures. The direction of fractures is controlled by the maximum principal stress.

In general, the propagation mode is different under the action of different principal stress differences. Under the condition of the principal stress difference is small, multiple hydraulic fractures easily form and radiate. Under the condition of the principal stress difference is large, the hydraulic fracture is relatively single. With the increase in the principal stress difference, the hydraulic fractures showed the following trend: the number of hydraulic fractures becomes single from multiple, and the propagation direction gradually shifts from more divergence to the direction of maximum principal stress.

4.2 Numerical simulation of two-hole synchronous hydraulic fracturing

To explore the propagation law in the process of synchronous hydraulic fracturing of two holes, a model of 300 mm × 300 mm × 10 mm is established. Two injection holes are set in the centre of the model, with a radius of 10 mm. The bond parameters are shown in Table 4. The fluid was injected at a rate of 33 m/s. Three different conditions, which include different hole arrangement modes, hole spacings and principal stress differences, are considered. We used the azimuth angle to represent the arrangement of double

Table 5 Hydraulic fracturing experimental conditions

Factors	Azimuth angle (°)	Spacing (mm)	σ_1(MPa)	σ_3(MPa)	$\sigma_1 - \sigma_3$(MPa)
Azimuth angle	0	20	20	4	16
	45	20	20	4	16
	90	20	20	4	16
Spacing	45	20	4	4	0
	45	40	4	4	0
	45	60	4	4	0
$\sigma_1 - \sigma_3$	45	40	4	4	0
	45	40	12	4	8
	45	40	20	4	16

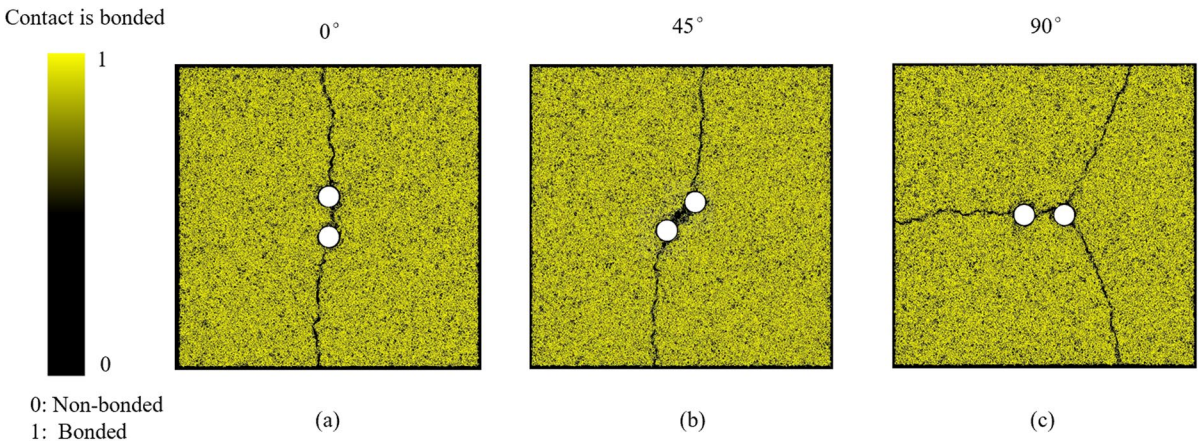

Fig. 11 The propagation pattern of fracture in different hole arrangement modes

holes. The azimuth angle refers to the angle between the direction of the maximum principal stress and the direction of the double hole arrangement. Figure 10 shows the schematic diagram of the three different hole arrangement modes. The numerical simulation conditions of the three different factors are shown in Table 5.

4.2.1 Effect of different hole arrangement modes

Figure 11 shows the pattern of hydraulic fracture propagation in various hole arrangement modes. It can be observed that different hole arrangement modes cause different propagation patterns of fractures. Hydraulic fractures develop along the direction of double hole arrangement under the condition of the azimuth angle is 0°. The hydraulic fracture initially expands in the direction of the double-hole arrangement before gradually deflecting in the direction of maximum principal stress as the azimuth angle increases. When the azimuth angle was 90°, two hydraulic fractures are developed from the right hole, and only one hydraulic fracture appears in the left hole, which is caused by the small spacing between holes. It can be revealed that the complexity of hydraulic fractures is consistent with the increase of azimuth. In other words, the complex hydraulic fractures typically appear when a certain angle exists between the maximum principal stress and the double-hole arrangement.

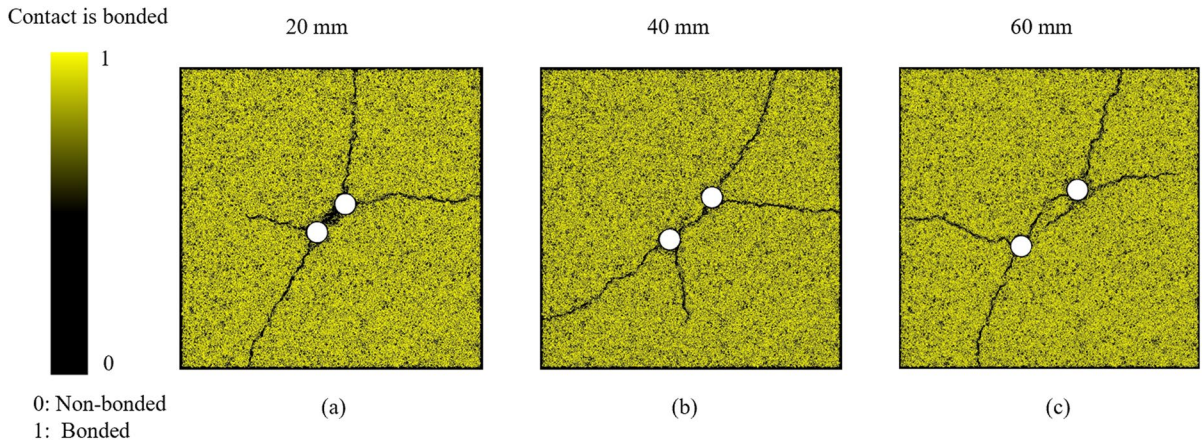

Fig. 12 The propagation pattern of hydraulic fractures in different hole spacings

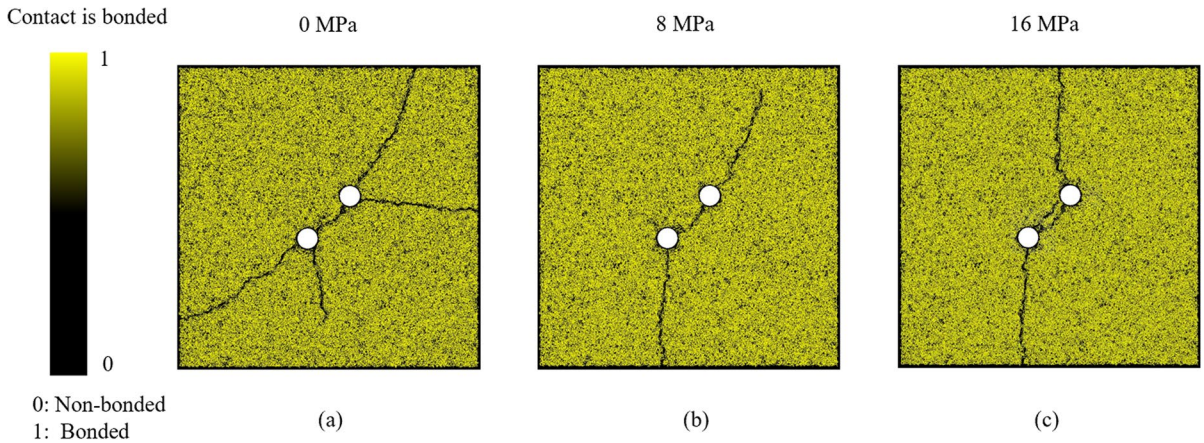

Fig. 13 The propagation pattern of hydraulic fractures in different principal stress differences

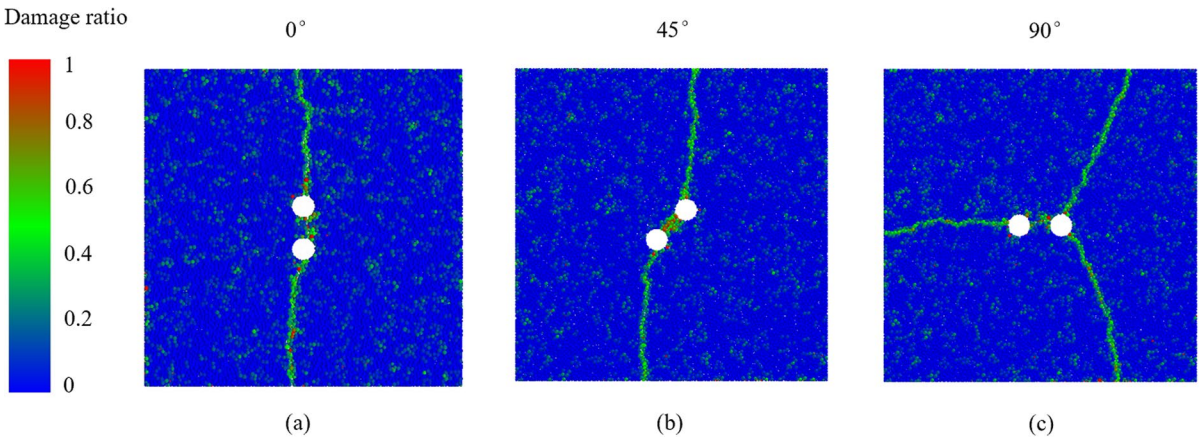

Fig. 14 Damage ratio of rock in different hole arrangement modes

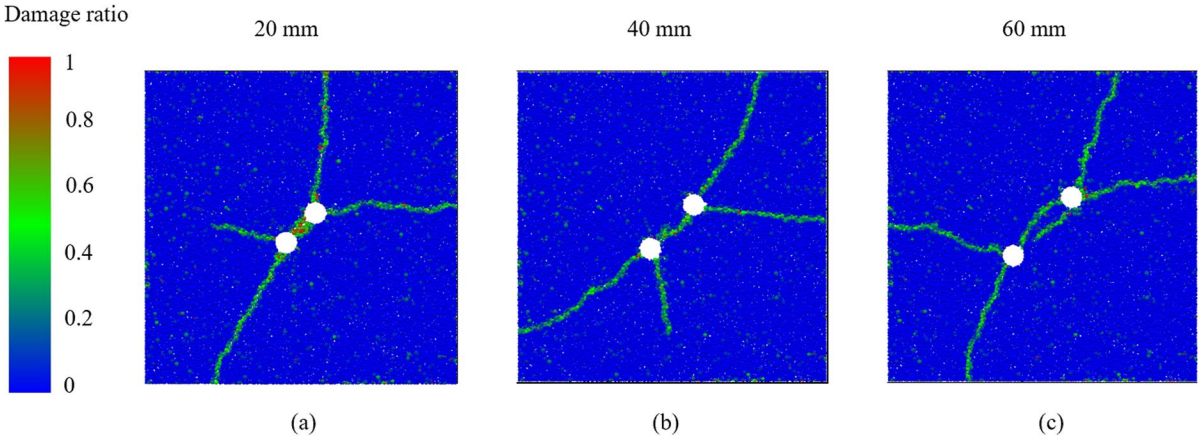

Fig. 15 Damage ratio of rock in different hole spacings

4.2.2 Effect of different hole spacings

Figure 12 shows the propagation pattern of fractures in various hole spacings. Complex fractures appear in three different cases. The outwards extending hydraulic fractures show similar characteristics. However, the hydraulic fracture propagation modes were still different. When the spacing between two holes was 20 mm, the rock between two holes was completely broken. The increase of spacing will reduce the damage degree of rock between two holes. When the distance between two holes was 40 mm, there was only one obvious hydraulic fracture between the two holes. Under the condition of the distance between two holes is 60 mm, two hydraulic fractures can be found between the two holes.

The above phenomena demonstrate that when the spacing between two holes is small, the stress superposition effect between two holes is obvious. This will lead to severe damage of the rock mass between holes. The stress superposition effect decreases, with the increase in the spacing. Within a certain spacing, the hydraulic fracture between the two holes intersects, and only one hydraulic fracture is formed between the two holes. When the spacing between the two holes exceeds a certain distance, the hydraulic

cracks developed between the two holes will not intersect into one. There will be two or even more. The fractures not only extend between the two holes but also extend to the edge of the sample.

4.2.3 *Effect of different principal stress differences*

Figure 13 depicts the pattern of hydraulic fracture propagation under various principal stress differences. The fractures are complex when the principal stress difference is 0 MPa. The hydraulic fracture propagation direction changes as a result of the increase in principal stress difference. This shows that the expansion form of hydraulic fractures presents the same law as that of single-hole injection hydraulic fracturing.

From the above analysis, it can be found that the fracture propagation trend of two-hole synchronous hydraulic fracturing is controlled by the principal stress. The hydraulic fracture is affected by the relative position and spacing of the two holes in the condition of the principal stress difference is 0 MPa. With an increase in the principal stress difference, the hydraulic fracture propagation direction is dominated by the principal stress difference.

4.2.4 *Damage ratio of rock*

To better reflect the damage degree of rock, the damage ratio, which is defined as the ratio of the broken bonds to the initial bonds, is introduced (Thornton et al. 1996; Wang et al. 2022).

$$D_r = \frac{B_0 - B}{B_0} \tag{41}$$

where D_r is the damage ratio ($D_r = 1$ indicates all the bonds are broken), B and B_0 are the number of bonds connect to particles at the current time step and the bond time.

Figures 14, 15 and 16 show the damage ratio of rock in different factors. Combined with Figs. 11, 12 and 13, it can be clearly observed that the colour of the particles at the position of the hydraulic fracture was green or red. When the rock was completely broken, such as the rock between two holes in Fig. 14b, the colour of the particles changes to red. Additionally, the colour of particles at nonfractures was mostly blue, and a few are green or red, which means that there is slight local damage in rock samples during hydraulic fracturing.

5 Conclusion

In this work, the EBPM is coupled with CFD to establish the hydraulic fracturing model. The feasibility of the hydraulic fracturing model is verified by considering the fracture propagation law under different principal stress differences. Numerical simulations of two-hole hydraulic fracturing are carried out. The effects of different hole arrangement modes, spacings between two holes and principal stress differences are studied. Essential conclusions are as follows:

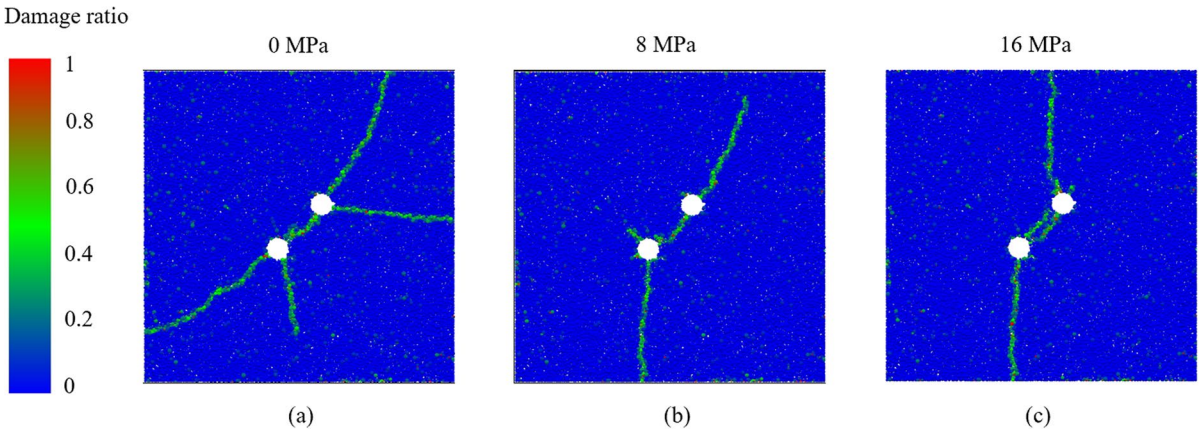

Fig. 16 Damage ratio of rock in different principal stress differences

(1) The arrangement of double holes will affect the complexity and expansion direction of hydraulic fractures. When the arrangement direction of two holes was consistent with the direction of maximum principal stress, the hydraulic fracture was relatively single. The complex hydraulic fractures typically appear when a certain angle exists between the maximum principal stress, especially at 90°.
(2) When the spacing between two holes is small, the stress superposition effect between the two holes is obvious, and the rock between the two holes is easily damaged. With the increase in the spacing, the stress superposition effect decreases. Within a certain spacing, only one hydraulic fracture is formed between the two holes. When the spacing between the two holes exceeds a certain distance, the hydraulic fractures developed between the two holes will be two or more. The fractures not only extend between the two holes but also extend to the edge of the sample.
(3) The principal stress controls the overall trend of fracture propagation in two-hole synchronous hydraulic fracturing. Under the condition of the principal stress difference is 0 MPa, the hydraulic fracture is affected by the relative position of two holes and the spacing between two holes. With an increase in the principal stress difference, the hydraulic fracture propagation direction is dominated by the principal stress difference.

Acknowledgements The authors acknowledge the financial support by the National Natural Science Foundation of China (52034010; 51979281; 51909146; 42072163). This work is also supported by Shenzhen Fundamental Research Program JCYJ20220530141016036, RCBS20200714114910354, and Shandong Overseas Excellent Yougth Research Fund 2022HWYQ-020.

Author contributions All authors read and approved the final manuscript.

Declarations

Competing interest The authors declare no conflicts of interest.

References

Brown NJ, Chen JF, Ooi JY (2014) A bond model for dem simulation of cementitious materials and deformable structures. Granul Matter 16:299–311. https://doi.org/10.1007/s10035-014-0494-4

Brown NJ (2013) Discrete element modelling of cementitious materials. PH.D. The University of Edinburgh

Cheng Y, Zhang Y, Yu Z, Hu Z, Yang Y (2020) An investigation on hydraulic fracturing characteristics in granite geothermal reservoir. Eng Fract Mech 237:107252. https://doi.org/10.1016/j.engfracmech.2020.107252

Detournay E (2016) Mechanics of hydraulic fractures. Annu Rev Fluid Mech 48:311–339. https://doi.org/10.1146/annurev-fluid-010814-014736

Duan K, Kwok CY, Wu W, Jing L (2018) DEM modeling of hydraulic fracturing in permeable rock: influence of viscosity, injection rate and in situ states. Acta Geotech 13:1187–1202. https://doi.org/10.1007/s11440-018-0627-8

Duan K, Kwok CY, Zhang Q, Shang J (2020) On the initiation, propagation and reorientation of simultaneously-induced multiple hydraulic fractures. Comput Geotech 117:103226. https://doi.org/10.1016/j.compgeo.2019.103226

Geertsma J, De Klerk F (1969) A rapid method of predicting width and extent of hydraulically induced fractures. J Petrol Technol 21:1571–1581. https://doi.org/10.2118/2458-PA

Gidaspow D (1994) Multiphase flow and fluidization: continuum and kinetic descriptions. Academic Press, San Diego, pp 239–353

Hertz BH (1882) On the contact of elastic solids. J Reine Angew Math 1882:156–171

Hubbert MK, Willis DGW (1957) Mechanics of hydraulic fracturing. Trans AIME 18:369–390

Khristianovich SA, Zheltov YP (1955) Formation of vertical fractures by means of highly viscous liquid. In: 4th World Petroleum Congress 2:579–586

Krzaczek M, Nitka M, Kozicki J, Tejchman J (2020) Simulations of hydro-fracking in rock mass at meso-scale using fully coupled DEM/CFD approach. Acta Geotech 15:297–324. https://doi.org/10.1007/s11440-019-00799-6

Lei B, Li H, Zuo J, Liu H, Yu M, Wu G (2021) Meso-fracture mechanism of longmaxi shale with different crack-depth ratios: experimental and numerical investigations. Eng Fract Mech 257:108025. https://doi.org/10.1016/j.engfracmech.2021.108025

Li YM (2020) Simulation of the interactions between multiple hydraulic fractures and natural fracture network based on discrete element method numerical modeling. Energy Sci Eng 8:2922–2937. https://doi.org/10.1002/ese3.712

Li BQ, Gonçalves da Silva B, Einstein H (2019) Laboratory hydraulic fracturing of granite: acoustic emission observations and interpretation. Eng Fract Mech 209:200–220. https://doi.org/10.1016/j.engfracmech.2019.01.034

Li ZQ, Li XL, Yu JB, Cao WD, Liu ZF, Wang M, Liu ZF, Wang XH (2020) Influence of existing natural fractures and beddings on the formation of fracture network during hydraulic fracturing based on the extended finite element method. Geomech Geophys Geo 6:58. https://doi.org/10.1007/s40948-020-00180-y

Liu HH, Ranjith PG, Georgi DT, Lai BT (2016) Some key technical issues in modelling of gas transport process in shales: a review. Geomech Geophys Geo 2:231–243. https://doi.org/10.1007/s40948-016-0031-5

Liu P, Ju Y, Feng Z, Mao L (2021a) Characterization of hydraulic crack initiation of coal seams under the coupling effects of geostress difference and complexity of pre-existing natural fractures. Geomech Geophys Geo 7:91. https://doi.org/10.1007/s40948-021-00288-9

Liu W, Yao J, Zeng Q (2021b) A numerical hybrid model for non-planar hydraulic fracture propagation in ductile formations. J Petrol Sci Eng 196:107796. https://doi.org/10.1016/j.petrol.2020.107796

Mindlin RD (1949) Compliance of elastic bodies in contact. J Mech 16:259–268

Mindlin RD, Deresiewicz H (1953) Elastic spheres in contact under varying oblique forces. J Mech 20:327–344. https://doi.org/10.1115/1.4010702

Ni T, Pesavento F, Zaccariotto M, Galvanetto U, Zhu QZ, Schrefler BA (2020) Hybrid FEM and peridynamic simulation of hydraulic fracture propagation in saturated porous media. Comput Method Appl M 366:113101. https://doi.org/10.1016/j.cma.2020.113101

Nordgren RP (1972) Propagation of a vertical hydraulic fracture. SPE J 12:306–314. https://doi.org/10.2118/3009-PA

Perkins TK, Kern LR (1961) Widths of hydraulic fractures. J Petrol Technol 13:937–949. https://doi.org/10.2118/89-PA

Rueda J, Mejia C, Quevedo R, Roehl D (2020) Impacts of natural fractures on hydraulic fracturing treatment in all asymptotic propagation regimes. Comput Method Appl M 371:113296. https://doi.org/10.1016/j.cma.2020.113296

Shi X, Han L, Han Q, Xiao C, Feng Q, Wang S, Du Y (2021) Experimental near-wellbore hydraulic fracture initiation and growth for horizontal wells with in-plane perforations. J Nat Gas Sci Eng 95:104224. https://doi.org/10.1016/j.jngse.2021.104224

Thornton C, Yin KK, Adams MJ (1996) Numerical simulation of the impact fracture and fragmentation of agglomerates. J Phys D Appl Phys 29:424

Timoshenko SP (1922) X. On the transverse vibration of bars of uniform cross-section. Philos Mag 43:125

Wang B, Zhou F, Wang D, Liang T, Yuan L, Hu J (2018) Numerical simulation on near-wellbore temporary plugging and diverting during refracturing using XFEM-based CZM. J Nat Gas Sci Eng 55:368–381. https://doi.org/10.1016/j.jngse.2018.05.009

Wang LG, Ge R, Chen X (2022) Establishing an oblique impact breakage master curve using a DEM bonded contact model. Comput Geotech 145:104668. https://doi.org/10.1016/j.compgeo.2022.104668

Xu T, Ranjith PG, Au ASK, Wasantha PLP, Yang TH, Tang CA, Liu HL, Chen CF (2015) Numerical and experimental investigation of hydraulic fracturing in kaolin clay. J Petral Sci Eng 134:223–236. https://doi.org/10.1016/j.petrol.2015.08.003

Xu T, Zhou G, Heap MJ, Yang S, Konietzky H, Baud P (2018) The modeling of time-dependent deformation and fracturing of brittle rocks under varying confining and pore pressures. Rock Mech Rock Eng 51:3241–3263. https://doi.org/10.1007/s00603-018-1491-4

Xu T, Fu TF, Heap MJ, Meredith PG, Mitchell TM, Baud P (2020) Mesoscopic damage and fracturing of heterogeneous brittle rocks based on three-dimensional polycrystalline discrete element method. Rock Mech Rock Eng 53:5389–5409. https://doi.org/10.1007/s00603-020-02223-y

Yang W, Geng Y, Zhou Z, Li L, Ding R, Wu Z, Zhai M (2020) True triaxial hydraulic fracturing test and numerical simulation of limestone. J Cent South Univ 27:3025–3039. https://doi.org/10.1007/s11771-020-4526-4

Yang W, Li S, Geng Y, Zhou Z, Li L, Gao C, Wang M (2021) Discrete element numerical simulation of two-hole synchronous hydraulic fracturing. Geomech Geophys Geo 7:55. https://doi.org/10.1007/s40948-021-00257-2

Yew CH, Weng X (2014) Mechanics of hydraulic fracturing. Gulf Professional Publishing

Zhang Y, Zhao G (2019) A global review of deep geothermal energy exploration: from a view of rock mechanics and engineering. Geomech Geophys Geo 6:4. https://doi.org/10.1007/s40948-019-00126-z

Zhang GD, Sun SS, Chao K, Niu RB, Liu BJ, Li Y, Wang F (2019) Investigation of the nucleation, propagation and coalescence of hydraulic fractures in glutenite reservoirs using a coupled fluid flow-DEM approach. Powder Technol 354:301–313. https://doi.org/10.1016/j.powtec.2019.05.073

Zheng H, Pu C, Sun C (2020a) Study on the interaction between hydraulic fracture and natural fracture based on extended finite element method. Eng Fract Mech 230:106981. https://doi.org/10.1016/j.engfracmech.2020a.106981

Zheng H, Pu C, Wang Y, Sun C (2020b) Experimental and numerical investigation on influence of pore-pressure distribution on multi-fractures propagation in tight sandstone. Eng Fract Mech 230:106993. https://doi.org/10.1016/j.engfracmech.2020b.106993

Zhou GL, Xu T, Konietzky H, Zhu W, Heng Z, Yu XY, Zhao Y (2022) An improved grain-based numerical manifold method to simulate deformation, damage and fracturing of rocks at the grain size level. Eng Anal Bound Elem 134:107–116. https://doi.org/10.1016/j.enganabound.2021.10.005

Zou J, Jiao Y, Tang Z, Ji Y, Yan C, Wang J (2020) Effect of mechanical heterogeneity on hydraulic fracture propagation in unconventional gas reservoirs. Comput Geotech 125:103652. https://doi.org/10.1016/j.compgeo.2020.103652